www.amlett.com, www.vbripress.com/aml, DOI: 10.5185/amlett.2014.nib503 Published online by the VBRI press in 2014

Structural and optical study of MeV cobalt ion implanted silicon

Pramita Mishra[1*], Vanaraj Solanki[1], Ashutosh Rath[2], Soumee Chakraborty[3], Himanshu Lohani[1], Pratap K. Sahoo[4], Biju Raja Sekhar[1]

[1]*Institute of Physics, Sachivalaya Marg, Bhubaneswar 751005, Odisha India*
[2]*Department of Materials Engineering, Indian Institute of Science, Bangalore, India*
[3]*Condensed Matter Physics Division, Indira Gandhi Centre for Atomic Research, Kalpakkam, India*
[4]*School of Physical Sciences, National Institute of Education and Research, Bhubaneswar 751005, Odisha, India*

[*]Corresponding author. Tel: (+91) 674 2306472; E-mail: pramitam@iopb.res.in

Received: 27 November 2013, Revised: 20 April 2014 and Accepted: 26 May 2014

ABSTRACT

We report the optical tunability through defect states created in silicon by 1 MeV cobalt ion implantation at room temperature in the fluence range of 5×10^{13} to 5×10^{15} ions cm^{-2}. Atomic force microscopy studies reveal the surface nanostructures with maximum roughness of 0.9 nm at a critical fluence of 5×10^{15} ions cm^{-2} which is reduced to 0.148 nm with further increase of fluence. The enhanced native oxide layers after Co ion implantation observed from X-Ray photoelectron spectroscopy studies confirm the presence of surface defects. The combined effect of nanostructures formation and amorphization leads to band gap tailoring. For low fluence, the nanostructures produced on the surface result in an enhanced absorption in the entire UV-Visible region with a simultaneous reduction in band gap of 0.2 eV in comparison to pristine Si whereas high fluence implantation results in interference fringes which signifies the enhancement in refractive index of the top implanted layer ensuing increase in band gap of 0.3 eV. Combined amorphous and crystalline phases of nanostructured surface with tunable optical absorption may have potential applications in solar cell, photovoltaics and optical sensors. Copyright © 2014 VBRI press.

Keywords: Nanostructures; amorphization; Raman spectroscopy; XPS absorbance.

Pramita Mishra is presently working as a research scholar in Institute of Physics, Bhubaneswar. Her research interest includes ion beam induced material modification and electronic structure of materials probed using photoemission.

Ashutosh Rath obtained his Ph.D. from Institute of Physics, Bhubaneswar, India in 2012. He currently holds the position of Research Associate in Department of Materials Science and Engineering, University of Wisconsin-Madison, USA. His research interest includes Nanostructures, metal/semiconductor interfaces and electron microscopy.

B. R. Sekhar is currently professor in Institute Of Physics, Bhubaneswar. His research interest includes material modification via ion beams and photoemission spectroscopy on strongly correlated electronic systems.

Introduction

The reduced dimensions and enhanced surface to volume ratio of nanoparticles lead to interesting chemical and physical properties much different from its bulk counterparts, which can be harnessed in technological applications. The enhanced optical and electronic properties of nanostructured silicon in comparison to bulk silicon **[1-3]** has created an upsurge of research in this arena, with an aim to build various silicon based multifunctional photonic and optoelectronic devices. Ion implantation is a versatile tool in Si-based technology involving VLSI applications. The controlled synthesis of

 Copyright © 2014 VBRI Press

nanostructures using ion beam technique has become an important processing tool to create non equilibrium phases with novel physical properties. The control over the number of ions implanted offers a unique possibility in creation of large area nanostructures and provides great flexibility in development of ion beam induced tunable optical and physical properties. In addition to creation of doped layers and production of defects within the host material, MeV ion implantation can also significantly modify the surface of the material by creation of patterned nanostructures via electronic and nuclear energy loss processes **[4]**. In case of low MeV ion implantation, both electronic and nuclear energy losses contribute to surface and matrix modifications. Hence, in recent times, implantation at MeV energies has emerged as a preferential tool for precise positioning of dopants, creation of point defects, production of amorphous layers and isolation structures through buried layers **[5]**. The evolution of dual amorphous and nano/micro-crystalline phases after ion implantation **[6]** is a promising candidate in solar cell industry due to its low cost, enhanced efficiency and improved stability in comparison to crystalline and amorphous silicon **[7]**. MeV magnetic ion implantation (Co, Mn, Ni) in silicon with varying fluences can also create a modified system with unique magnetic and optical properties **[8, 9]** due to the embedded magnetic nanoparticles in silicon matrix.

In the present work, we emphasize on nanostructuring and amorphization of silicon surfaces, achieved via 1 MeV cobalt ion implantation, at varying fluences. Ion beam implantation leads to creation of mixed amorphous and crystalline phase within the Si matrix, which is evidenced from Raman Spectroscopy and X-Ray Diffraction (XRD) study. The surface modifications due to ion implantation were studied by Atomic Force Microscopy (AFM) and X-ray Photoelectron Spectroscopy (XPS). Implantation induced defects and damage in the bulk silicon with simultaneous generation of surface nanostructures lead to changes in the structural and optical properties of the samples. The mechanisms involved in the evolution of physical and optical properties of implanted silicon are explained in connection with MeV ion implantation. The competition between defect generation and damage induced amorphization leads to a fluence dependent change in the structural and optical properties of the system.

Experimental

The singly charged cobalt ion implantation on commercially available single crystal silicon (p-Si (100)) with 1 MeV energy has been carried out at room temperature using the implantation beamline of the 3 MV Tandem Pelletron accelerators at Institute of Physics. The implantation experiment was performed at a base pressure of 1×10^{-6} mbar at an angle of ~7° with respect to the sample normal to avoid the channeling effect. The fluence for irradiation was varied in the range of 5×10^{13} ions cm^{-2} to 5×10^{15} ions cm^{-2}. The Atomic Force Microscope (AFM, Nanoscope V), in tapping mode, was utilized to study the morphological changes after irradiation. The structural investigations were performed using X-ray diffraction (XRD) method by utilizing Cu Kα source (Bruker system). In order to study the structural changes, the 514.5 nm line of an Argon ion laser was used and the scattered light was collected by a Renishaw (model InVia) Raman spectrometer and recorded using an air cooled charge coupled device (CCD). Shimadzu spectrophotometer was utilized to study reflectance in wavelength range of 200 nm – 2000 nm. The change of the surface chemical state after ion implantation was studied by X-ray photoelectron spectroscopy (XPS) using a concentric hemispherical analyzer at constant analyser energy (CAE) mode using pass energy of 20 eV.

Results and discussion

The surface morphology of the pristine and implanted samples as characterized by AFM is shown in **Fig. 1 (a-e)**. The surface of pristine sample is very smooth with a root mean square (rms) roughness of 0.09 nm (**Fig 1(a)**). Ion implantation with fluences of 5×10^{13} and 5×10^{14} ions cm^{-2} (**Fig. 1(b, c)**) leads to the formation of silicon oxide nanostructures with average sizes of 30 nm and 50 nm, respectively. Further increasing the ion fluence gives rise to surface smoothening (**Fig. 1(d, e)**). The plot of roughness as a function of irradiation fluence (**Fig. 1(f)**), shows the roughness increase upto a critical fluence 5×10^{14} ions cm^{-2} (shown by dotted line), and later it decreases.

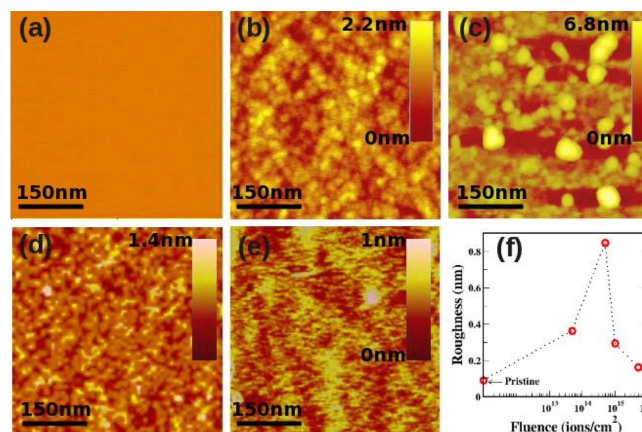

Fig. 1. AFM images (500nm X 500nm) of (a) pristine, (b) 5×10^{13}, (c) 5×10^{14} (d) 1×10^{15}, (e) 5×10^{15} ions cm^{-2} while (f) shows the variation of roughness as a function of implantation fluence. The z-scale and length scale are shown for the respective fluences.

The decrease in surface roughness beyond 5×10^{14} ions cm^{-2} is due to the predominant diffusion mechanism induced due to enhanced amorphization at higher fluences. The evolution of surface morphology of ion implanted surface is driven by a balance between surface roughening and smoothening processes **[10]**. A maximum in the value of surface roughness and hence grain size is obtained at 5×10^{14} ions cm^{-2} which is attributed to the transition from order driven crystalline regime at low fluence to the disorder driven amorphous regime at higher fluence. Similar types of transitions were reported by Voutsas et al. **[11]** in which the amorphous silicon was crystallized through annealing.

The XRD spectrum of pristine as well as ion implanted silicon is displayed in **Fig. 2.** The XRD spectrum of pristine silicon shows the Si (400) diffraction peak cantered at 69.37° with a Full width at half maximum (FWHM) of

Copyright © 2014 VBRI Press

0.04°. After implantation, even though there is no change in the peak position, the FWHM of (400) peak increased to ~0.06° for all fluences. During the MeV ion implantation, the energy transfer to the Si matrix via electronic and nuclear energy loss processes creates defects/vacancies and Si-Si bond breaks, which results in widening the FWHM in the XRD peak. The presence of broad Si(400) peak, after implantation, confirms the mixture of amorphous and crystalline phase in the silicon matrix after ion implantation.

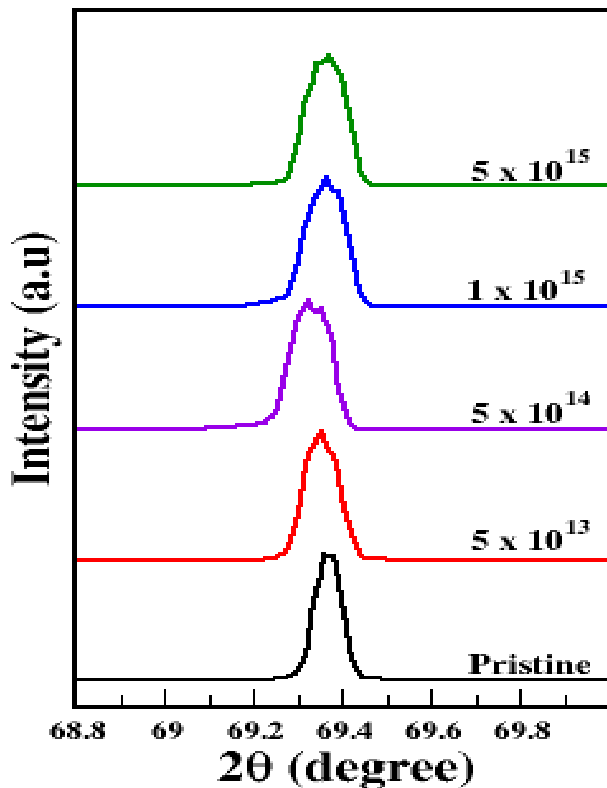

Fig. 2. XRD spectra of Si(400) peak for pristine as well as after implantation for different fluences.

Fig. 3(a) shows the Raman scattering spectra for pristine and implanted the samples. All the peaks are fitted with Lorentzian function to obtain the peak position and peak width. The Raman spectra of pristine sample shows Raman peaks ascribed to single crystal silicon centered at 242 cm^{-1} and 302 cm^{-1} (**Fig. 3(a)**) associated with Longitudinal optical (LO) and Longitudinal Acoustic (LA) phonon modes respectively while peak centered at 520.4 cm^{-1} corresponds to Transverse Optical (TO) phonons of crystalline silicon **[12]**. The implanted samples develop signal of amorphous silicon modes in addition to the reduced intensity of crystalline modes which gives an indication of transition from crystalline to amorphous phase. For implanted samples, the features emerge around 120 cm^{-1}, 380 cm^{-1} and 480 cm^{-1} which corresponds to the Transverse Acoustic (TA), LO and TO modes of amorphous Silicon (a-Si) respectively **[11]**. With increase in ion fluence the position of a-Si TO peak shifts to lower wave number with an enhanced intensity and FWHM which can be inferred from **Fig. 3(c)**. The position of TO modes of crystalline Silicon (appearing at 520.4 cm^{-1}) remains unaltered after implantation. The reduction in intensity and FWHM broadening of TO mode of a-Si with increasing ion fluence denotes the reduction in crystallinity due to amorphization induced by ion implantation.

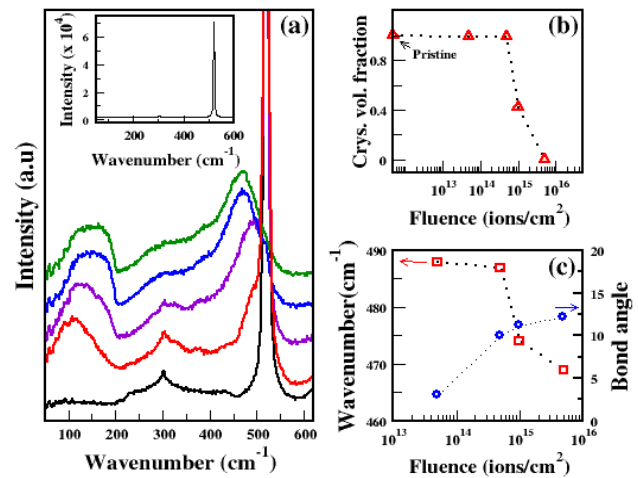

Fig. 3. (a) shows the Raman spectra for pristine (black) and after implantation with various fluences 5 × 10^{13} (red), 5 × 10^{14} (violet), 1 × 10^{15} (blue) and 5 × 10^{15} ions cm^{-2} (green). Inset shows the full Raman spectrum of (a) pristine sample, (b) The change in crystalline volume fraction after implantation and (c) shows the change in TO Raman modes of amorphous silicon (red square dots) and Si tetrahedral bond angle distortion (blue star dots) as a function of ion fluences.

The enhanced a-Si modes with reduced intensity of c-Si phonon modes at low fluences, suggests the presence of amorphous islands within Silicon single crystal. For the highest fluence implantation induced amorphization results in the decline of crystalline modes. The crystalline to amorphous ratio was obtained from the crystalline volume fraction ρ calculated using the formula adopted by Tsu et al. **[13]**

$$\rho = I_c / (I_c + \sigma_r I_a); \qquad (1)$$

where, σ_r implies ratio of integrated Raman backscattering cross section for amorphous to single crystalline silicon. The value of σ_r is taken as 0.08 **[13]** I_c and I_a are integrated intensity of crystalline and amorphous phases respectively. The plot of ρ vs fluence, displayed in **Fig. 3(b)** shows that the crystalline volume fraction reduces with increasing fluence and becomes zero for the highest fluence symbolizing a continuous transformation from crystalline to amorphous regime with varying ion fluences. The amount of disorder present in the silicon matrix can be inferred from the FWHM of a-Si TO phonon peak. The amorphous silicon peak gives an indication of the amount of disorder with respect to fluence. In crystalline silicon the tetrahedral bond angle between Si-Si bonds is fixed at 109° 28'. Implantation results in the breakage of bonds which leads to an amorphous system consisting of a distribution of bond angles varying from 3° to 13°. The deviation of bond angle from crystalline silicon quantifies the amount of disorder in the system. The relation between the full width at half maximum (FWHM), Γ(cm^{-1}), of the amorphous peak and the bond angle deviation Δθ (degree) is given by the following equation **[14]**,

Copyright © 2014 VBRI Press

$$\Gamma/2 = 7.5 + 3\Delta\theta \qquad (2)$$

The calculated bond angle deviation vs fluence is displayed in **Fig. 4(b)**. The bond angle deviation increases from 3° for sample implanted with a fluence of 5×10^{13} ions cm^{-2} to 12.2° for the sample implanted with the highest fluence. Bond angle deviation within the range $0° < \Delta\theta \leq 7°$ is in the transition regime of amorphous to crystalline phase **[14]** while the value of $\Delta\theta$ greater than 7° is a signature of the presence of amorphous complexes **[15]**. Thus, initial implantation leads to the presence of small amount of amorphous phase in a crystalline matrix and hence smaller bond angle deviation while increasing the implantation fluence leads to an enhancement in amorphization with an increasing bond angle deviation.

The distribution of Cobalt ions and defects for 1 MeV Cobalt ions in Silicon calculated from Stopping and Range of Ions in Matter (SRIM) **[16]** is presented in **Fig. 4**. The projected range (R_P) of 1 MeV Cobalt ions in Silicon is around 840 nm (shown by dotted line in **Fig. 4(a)**). Energetic ion interaction with the host atoms lead to different complex phenomena which include defect creation in the bulk and change in the surface topography. Defects are generated in non-equilibrium conditions, with ion bombardment which functions as indispensable processing steps either for growth of nanostructures or their device applications. Defects produced in the implanted layers control subsequent evolution of defects and extent of relaxation of the disordered layer. The topographical evolution of solid surface during implantation is driven by the competition between surfaces roughening which occurs due to sputtering and surface smoothening induced by mass transport during surface diffusion. When an energetic ion travels through the solid, it loses its energy via nuclear energy loss S_n and electronic energy loss S_e. The former is related to the direct transfer of ion energy to target atoms through elastic collisions while latter is related to the electronic excitations and ionization of target atoms via inelastic collisions.

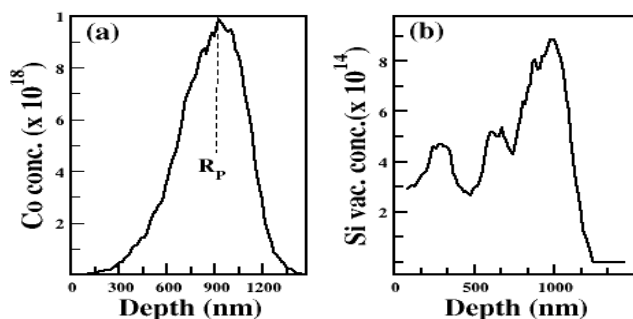

Fig. 4. The SRIM calculation of (a) Co range profile and (b) Si vacancies concentration for 1 MeV Co ions in Si.

For 1 MeV Cobalt ion in Silicon, the calculated values of S_e and S_n are ~ 70.6 eV/Å and 39.6 eV Å respectively. Due to the lower Se/Sn ratio (~ 1.8) both the types of energy loss mechanisms govern the surface modifications at the energy we deal with in this paper. Cobalt ion impinging on silicon produces vacancies and interstitials in the silicon matrix. Ion implanted in a semiconductor produces vacancies and interstitials, with vacancies predominantly located near the surface and interstitials near the implanted zone **[17]**. With increasing ion fluence, beam induced thermal effects shall result in an enhanced diffusion of Cobalt interstitials into the bulk owing to the high diffusion coefficient of cobalt ions in Silicon. The plot of vacancy creation during implantation as a function of depth, shown in **Fig. 4(b)**, reveals that the amount of Silicon defects created near the surface region is comparatively lower in magnitude than near the end of range of the Cobalt ions. The signature of amorphization in Raman spectra and peak broadening in XRD spectra correlates with the defect formation in SRIM calculations.

Fig. 5 shows the Si 2p core level XPS spectra of the pristine and ion implanted samples. The Si 2p spectra is fitted by a superposition of 5 Gaussian-Lorentzian lines (Si^{n+} where n = 0, 1, 2, 3 and 4). The core level spectrum of pristine sample shows the main feature Si^0 centered around 97.8 eV associated with the $Si\text{-}Si_4$ tetrahedron. In addition to Si^0 line, the core-level spectra also consist of Si suboxides centered at 98.7, 99.6, 101.4 and 102.6 eV corresponding to Si^{1+}, Si^{2+}, Si^{3+} and Si^{4+}, respectively. After implantation, the intensity of Si^0 peak decreases with a simultaneous increase in the intensity of SiO_x states suggesting the formation of silicon oxide at the near surface region.

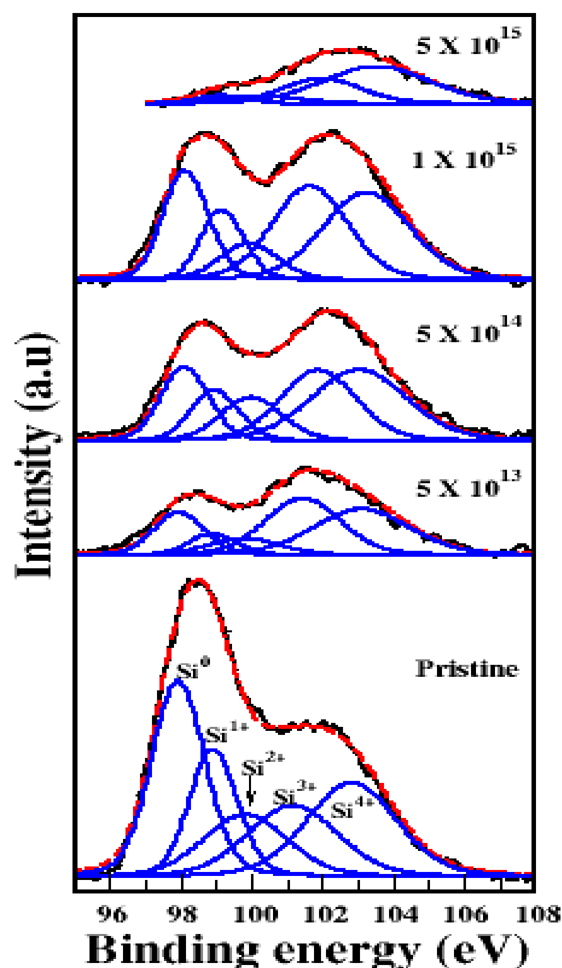

Fig. 5. Si 2p core level XPS spectra of pristine and after implantation samples with various fluences (black curve denotes raw spectra while red denotes the fitted spectra). The fitting for various charge states of Si^{n+} (n = 0 – 4) are shown as blue lines.

Copyright © 2014 VBRI Press

The peak area ratio of Si^0 to SiO^{n+} (n = 1-4) calculated from XPS (**Fig. 6**) indicates the increase in amount of oxygen content in samples due to implantation. The ratio of Si/SiO_x decreases from 0.4 for pristine to ~zero for 5×10^{15} ions cm^{-2} implanted sample. Even in high purity floating zone silicon, oxygen occupying interstitial sites (O_i) is a dominating impurity with a typical concentration in the range of 10^{15} cm^{-3} **[18]**. When the covalent bond between the two Si atoms is broken, two bonding electrons are released which induces the formation of two Si-O bonds bridging the broken Si-O bond **[19]**. Due to implantation, the surface Si-Si bonds break and thus the oxygen atoms occupying preferentially an interstitial position, bonds to two neighboring Si atoms and act as traps for migrating vacancies. This leads to an increase in SiO_x content for the implanted samples confirming the enhancement of bond breakage induced damage in the surface region of the implanted samples. This is in agreement with the AFM results that the observed nanostructures on the implanted surfaces are likely to be SiO_x.

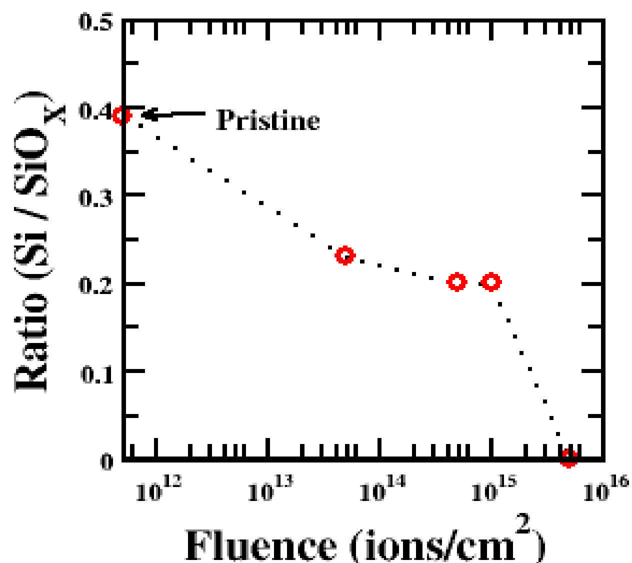

Fig. 6. The ratio of Si/SiO_x as a function of implantation fluence.

The absorbance spectrum of pristine sample (**Fig. 7**) shows the direct optical transition centred around 360 nm. There occurs a reduction in intensity of the direct optical edge, for all fluences, which suggests the ion beam induced amorphization **[20]**. After ion implantation with fluence 5×10^{13} and 5×10^{14} ions cm^{-2}, the absorption is enhanced in the entire UV-Vis region, compared to the pristine sample. However, for higher fluences (1×10^{15} and 5×10^{15} ions cm^{-2}), the absorbance is higher in the UV region but it is considerably lower in the visible region. As observed from AFM study, the sizes of the nanostructures are 30 and 50nm for implantation fluence 5×10^{13} and 5×10^{14} ions cm^{-2}, respectively. It is expected that the nanostructures with smaller size, with large surface area, can absorb more light, due to light trapping effect **[21]**, than larger nanostructures accounting for the observed absorbance seen in the present study. For higher fluences, the ion beam induced amorphization leads to reduction in the visible absorbance whereas the increased absorbance in UV region may be due to the formation of cobalt nanoparticles as observed by Zhang. et. al **[22]** and Farhadi. et. al **[23]**. The size of the nanostructures, amorphization and formation of Co nanoclusters during implantation collectively lead to the absorbance behaviour shown here.

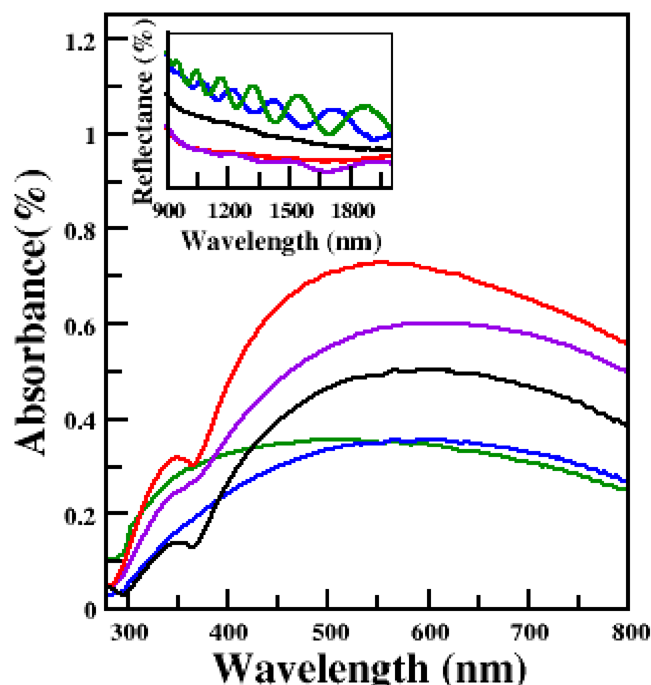

Fig. 7. Absorbance spectra of pristine (black) and after implantation with various fluences 5×10^{13} (red), 5×10^{14} (violet), 1×10^{15} (blue) and 5×10^{15} ions cm^{-2} (green). Inset shows the respective reflectance spectra in the IR region.

The inset of **Fig. 7** shows the reflectance spectrum in the InfraRed (IR) range. Samples with implantation fluence beyond 5×10^{13} ions cm^{-2} exhibit oscillatory behaviour. Fringe amplitude increases with increasing ion fluence and there is a shift in position of maxima and minima. High fluence implantation in silicon leads to a highly disordered implanted surface. The interference of light multiply-reflected between the front surface and the interface between the disordered and crystalline materials are given rise to an interference fringe pattern in the reflectance spectrum **[24]**. Implantation leads to amorphization of silicon single crystal and thus a change in the refractive index of the implanted layers which can be concluded from the Fresnel's Formula of interference. The effective thickness of the irradiated layer is calculated according to the formula

$$\eta L = N/(2\Delta\upsilon) \qquad (3)$$

where, N is the number of interference fringes between two maxima/minima η and L are the refractive index and width of the irradiated layer respectively $\Delta\upsilon$ is the change in wave number between the two maxima/minima corresponding to N number of fringes. The computed effective thickness is 3446, 4337 and 4853 nm for 5×10^{14}, 1×10^{15} and 5×10^{15} ions cm^{-2} respectively. As the mean layer thickness of the irradiated layer is nearly constant with ion fluence, it implies an increase in refractive index of the irradiated layer with an increasing ion fluence which results in an increase in the effective thickness **[25]**.

Copyright © 2014 VBRI Press

The Tauc plot of pristine sample **Fig. 8(a)** shows an indirect band gap of 1.11 eV. After implantation, with 5 × 10^{13}, 5 × 10^{14} ions cm^{-2}, the bandgap reduces to 0.9 and 1.0 eV, respectively while for higher fluences, there occurs an enhancement in the bandgap ~0.3 eV which can be inferred from **Fig. 8**. For lower implantation fluences, the formation of the SiO_x nanostructures (as seen from AFM), having mixture of crystalline and amorphous phases (as seen in Raman study), introduce the defect states and hence reduce the bandgap of silicon. However for higher fluences, the enhanced amorphization and strain reduction accompanied by structural relaxation leads to bandgap enhancement due to higher refractive index of SiO_x surface. The bandgap widening due to the creation of amorphized Si surface, having higher refractive index compared to pristine silicon, has been reported by Zamrnit. et al **[26]**. The absorbance studies thus show a fluence dependent transition from crystalline to amorphous regime where low fluence implantation leads to reduction in the band gap value while high fluence implantation leads to an enhancement in the band gap value in comparison to pristine silicon.

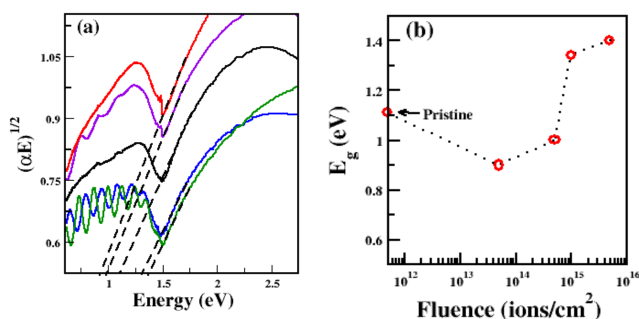

Fig. 8. (a) Tauc Plot of pristine (black) and after implantation with various fluences 5 × 10^{13} (red), 5 × 10^{14} (violet), 1 × 10^{15} (blue) and 5 × 10^{15} ions cm^{-2} (green) and (b) depicts the change in Bandgap (E_g) as a function of fluence.

In addition to the amorphization of the surface, the roughness of the surface can also play a crucial role in the bandgap variation. Luna López et al. **[27]** have reported the change in band gap with the corresponding change in roughness parameters, obtained from AFM study. They have shown that bandgap of the samples decrease when the roughness increase while a decreasing roughness results in an increased bandgap of the material. As seen in fig. 1(f), the roughness increases for lower fluences (5 × 10^{13} and 5 × 10^{14} ions cm^{-2}) and there after it decreases for higher fluences (1 × 10^{15} and 5 × 10^{15} ions cm^{-2}) which provides direct evidence about the dependency of bandgap variation, as seen in the Tauc plot, on the roughness parameter.

The enhanced light absorption over a broad range in low fluence implanted samples may be utilized in solar cell applications while the interference fringes observed in high fluence implanted samples can be used in optical sensors for detecting analytes (chemicals, biomolecules etc) by monitoring the shifts in the fringe pattern due to change in refractive index **[28]**. A mixture of amorphous and crystalline silicon has been created via ion implantation which can have potential applications in solar cells and photovoltaics.

Conclusion

The implantation of cobalt ions in Si(100) single crystal creates nanostructured surfaces with simultaneous generation of embedded and surface defects. XRD, XPS and Raman spectroscopy studies confirm the change in amorphization and defects as a function of fluences. A mixture of amorphous and crystalline silicon with tunable optical band gap has been observed due to the combined effect of nanostuctures formation and defect generation by implantation. Low fluence implantation leads to small sized nanostructures with an enhanced absorption over a broader region while high fluence implantation exhibits interference fringes in the NIR region. Fluence dependent optical properties are observed which can be exploited in Si based solar cells and optical sensing owing to the increased stability in comparison to amorphous Si.

Acknowledgements

We would like to thank Prof. Shikha Varma and Mr. Santosh Choudhury for XPS and AFM experiments. We would also like to thank Mr. Mohit Kumar for XRD and Absorbance experiments.

Reference

1. Chao, Y.; *Comprehens. Nanosci. Technol.* **2011**, *1*, 543. **DOI:** 10.1016/B978-0-12-374396-1.00039-8
2. Pavesi, L.; Gaburro, Z.; Bettotti, P.; Vijaya Prakash, G.; Cazzanelli, M.; Oton, C.J.; *Optics Lasers Eng.* **2003**, 39, 345. **DOI:** 10.1016/S0143-8166(01)00140-3
3. Stutzmann, M.; physica status solidi (b), **1995**, 192, 273. **DOI:** 10.1002/pssb.2221920205
4. Heinig, K. H.; Müller, T., Schmidt, B.; Strobel, M.; Möller, W.; *Appl. Phys A: Mat. Sc. Proc.* **2003**, *77*, 17. **DOI:** 10.1007/s00339-002-2061-9
5. Chason, E.; Picraux, S. T.; Poate, J. M.; Borland, J. O.; Current, M. I.; Rubia, T. D; Eaglesham, D. J.; Holland, O. W.; Law, M. E.; Magee, C. W.; Mayer, J. W.; Melngailis, J. ; Tasch, A. F.; *J. Appl. Phys.* 1997, *81*, 6513. **DOI:** 10.1063/1.365193
6. Dey, S.; Roy, C., Pradhan, A.; Varma, S.; *J. Appl. Phys.* **2000**, *87*, 1110. **DOI:** 10.1063/1.371987
7. Green, M.A.; *Mater. Sci. Eng. B*, **2000**, *74*, 118. **DOI:** 10.1016/S0921-5107(99)00546-2
8. Cattaruzza, E.; Gonella, F.; Mattei, G.; Mazzoldi, P.; Gatteschi, D.; Sangregorio, C.; Falconieri, M.; Salvetti, G.; Battaglin, G.;*Appl. Phys. Lett.* **1998**, *73*, 1176. **DOI:** 10.1063/1.122120
9. Niklasson, G. A.; Granqvist, C. G.; *J. Appl. Phys.* **1984**, *55*, 3382. **DOI:** 10.1063/1.333386
10. Eklund, E.A.; Snyder, E.J.; Williams, R.S.; *Surface Science,* **2003,** *285*, 157. **DOI:** 10.1016/0039-6028(93)90427-L
11. Voutsas, A. T.; Hatalis, M. K.; Boyce, J.; Chiang, A.; *J. Appl. Phys.* **1995**, *78*, 6999. **DOI:** 10.1063/1.360468
12. Kirillov, D.; Powell, R. A.; Hodul, D. T.; *J. Appl. Phys.* **1985**, *58*, 2174. **DOI:** 10.1063/1.335983
13. Tsu, R.; Gonzalez, H. J.; Chao, S. S.; Lee, S. C.; Tanaka, K.; *Appl. Phys. Lett.* **1982**, *40*, 534. **DOI:** 10.1063/1.93133
14. Beeman, D.; Tsu, R.; Thorpe, M. F.; *Phys. Rev. B,* **1985**, *32*, 874. **DOI:** 10.1103/PhysRevB.32.874
15. Motooka, T.; Kobayashi, F.; Fons, P.; Tokuyama, T.; Suzuki, T.; Natsuaki, N.; *Jpn. J. Appl. Phys*., **1991**, *30*, 3617. **DOI:** 10.1143/JJAP.30.3617
16. http:// www.srim.org.
17. Mazzone, A. M.; *Phys. status solidi (a)*, **1986**, *95*, 149. **DOI:** 10.1002/pssa.2210950118

 Copyright © 2014 VBRI Press

18. Lalita, J.; Keskitalo, N.; Hallén, A.; Jagadish, C.; Svensson, B.G.; *Nucl. Instr. and Meth.* B, **2006**, *120*, 27.
 DOI: 10.1016/S0168-583X(96)00474-0
19. Kaiser, W.; Keck, P. H.; Lange, C. F.; *Phys. Rev.* **1956**, *101*, 1264.
 DOI: 10.1103/PhysRev.101.1264
20. Jun, S.; Rack, P.D.; McKnight, T.E.; Melechko, A.V.; Simpson, M. L., *Appl. Phys. Lett.* **2006**, *89*, 022104.
 DOI: 10.1063/1.2219136
21. Liu, Y.; Ji, G.; Wang, J.; Liang, X.; Zuo, Z.; Shi, Y.; *Nano. Res. Lett.*, **2012**, *7*, 663.
 DOI: 10.1186/1556-276X-7-663
22. Zhang, Q; Chen,C.; Wang, M.; Cai, J.; Xu, J.; Xia, C.; Nano. Res. Lett., **2011**, *6*, 586.
 DOI: 10.1186/1556-276X-6-586
23. Farhadi, S.; Pourzare, K.; Sadeghinejad, S.; *J. Nanost. Chem*, **2013**, 3, 16.
 DOI: 10.1186/2193-8865-3-16
24. Hubler, G. K.; Waddell, C. N.; Spitzer, W. G.; Fredrickson, J. E.; Prussin, S.; *J. Appl. Phys.*, **1979**, *50*, 3294.
 DOI: 10.1063/1.326370
25. Wendler, E.; Peiter, G.; *J.Appl. Phys.* **2000**, *87*, 7679.
 DOI: 10.1063/1.373440
26. Zamrnit, U.; Madhusoodanan, K.N.; Marinelli, M.; Scudieri, F.; Pizzoferrato, R.; Mercuri, F.; Wendler, E.; Wesch, W.; *J. Phys*. IV France, **1994**, *04*, C7-113.
 DOI: 10.1051/jp4:1994728
27. López, J. A. L.; López, J. C.; Valerdi, D. E. V.; Salgado, G. G.; Díaz-Becerril, T.; Pedraza, A. P. ; Gracia, F. J. F.; *Nano. Res. Lett.* **2012**, *7*, 604
 DOI: 10.1186/1556-276X-7-604
28. Pacholski, C.; *Sensors,* **2013**, *13*, 4694
 DOI: 10.3390/s130404694

Advanced Materials Letters

Publish your article in this journal

ADVANCED MATERIALS Letters is an international journal published quarterly. The journal is intended to provide top-quality peer-reviewed research papers in the fascinating field of materials science particularly in the area of structure, synthesis and processing, characterization, advanced-state properties, and applications of materials. All articles are indexed on various databases including DOAJ and are available for download for free. The manuscript management system is completely electronic and has fast and fair peer-review process. The journal includes review articles, research articles, notes, letter to editor and short communications.

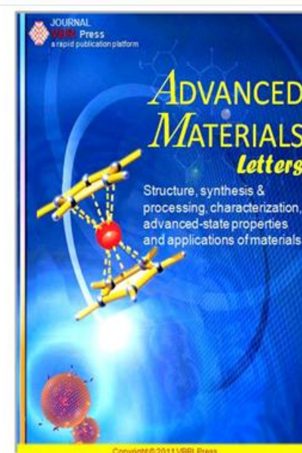

 Copyright © 2014 VBRI Press